Influence of temperature on the dissolution kinetics of synthetic LaPO4-monazite in acidic media between 50 and 130 °C

Yulia Arinicheva, Clémence Gausse, Stefan Neumeier, Felix Brandt, Konstantin Rozov, Stephanie Szenknect, Nicolas Dacheux, Dirk Bosbach, Guido Deissmann

Influence of temperature on the dissolution kinetics of synthetic $LaPO_4$-monazite in acidic media between 50 and 130°C

Yulia Arinicheva[1,2*], Clemence Gausse[3], Stefan Neumeier[1], Felix Brandt[1], Konstantin Rozov[1,4], Stéphanie Szenknect[3], Nicolas Dacheux[3], Dirk Bosbach[1], Guido Deissmann[1]

[1]Forschungszentrum Jülich GmbH, Institute of Energy and Climate Research (IEK-6): Nuclear Waste Management and Reactor Safety, 52425 Jülich, Germany

[2]Forschungszentrum Jülich GmbH, Institute of Energy and Climate Research (IEK-1): Materials Synthesis and Processing, 52425 Jülich, Germany

[3]ICSM, CNRS, CEA, ENSCM, Univ. Montpellier, Site de Marcoule, Bât 426, BP 17171, 30207 Bagnols/Cèze, France

[4]Institute of Environmental Geology, Russian Academy of Sciences, St. Petersburg State University, St. Petersburg 199004, Russia

*corresponding author.

E-mail address: y.arinicheva@fz-juelich.de (Y. Arinicheva).

Abstract

Single-phase monazite-type ceramics are discussed as waste forms for the safe disposal of surplus plutonium or separated minor actinides. To gain a deeper insight into the mechanism governing the dissolution of monazite-type compounds, the dissolution kinetics of synthetic $LaPO_4$-monazite was systematically studied by dynamic dissolution experiments carried out in the temperature range from 50 to 130°C in acidic media (0.01M HNO_3). The dissolution rates at far from equilibrium conditions increased from 3.2×10^{-5} g m^{-2} d^{-1} at 50°C to 2.5×10^{-4} g m^{-2} d^{-1} at 130°C. Two different temperature regions were observed, in which the normalised dissolution rates of $LaPO_4$ have a diverging temperature dependence, indicating two different mechanisms of dissolution: namely surface-controlled dissolution (T = 50 – 90°C; E_a = 44 kJ mol^{-1}) and transport-controlled dissolution (T = 90 – 130°C; E_a = 7.5 kJ mol^{-1}). Complementary thermodynamic modelling studies of the dissolution of $LaPO_4$ at the experimental conditions show that La-rhabdophane ($LaPO_4{\cdot}0.667H_2O$) is the thermodynamically favoured phosphate phase in aqueous environments below about 100°C. Apparently, the hydration of monazite and the formation of a thin surface layer consisting of rhabdophane is an intermediate step controlling the dissolution kinetics of the $LaPO_4$ monazite ceramics in low temperature aqueous environments.

Key words: monazite, nuclear waste form, dissolution kinetics, temperature dependence

1. Introduction

Disposal of high-level radioactive wastes in deep geological repositories in stable geological formations is generally considered as the safest and most sustainable solution for the management of these wastes, providing for a high-level of passive post-closure safety (IAEA, 2004; Council of the European Union, 2011; Ahn and Apted, 2011). The long-term containment and isolation of the wastes from the biosphere is generally ensured by a complementary and redundant system of engineered barriers including waste forms, waste containers, and backfill materials, in combination with a suitable repository host rock acting as geological barrier. In geological disposal facilities in crystalline or clay rocks the waste packages are generally expected to come into contact with groundwater in the long term, after resaturation of the repository. Even in repositories in salt rocks, the presence of water cannot be completely ruled out for less probable scenarios, for example, an early failure of shaft seals and plugs. After failure of the waste containers due to aqueous corrosion, radionuclides can be released from the degrading waste forms into the near-field water and subsequently migrate into the geo-/biosphere via the water pathway.

Thus insight into the aqueous durability of nuclear waste forms and the radionuclide source term are essential prerequisites for the long-term safety assessment of an underground repository, requiring a mechanistic understanding of the dissolution processes. The long-term performance of the waste forms in a deep geological repository and their aqueous durability are controlled to a varying degree by thermodynamics and reaction kinetics and can be affected by the near-field hydro-(geo)chemistry and the hydrodynamic regime. Geochemical conditions affecting waste form durability comprise in particular pH and redox conditions as well as ionic strength and composition of the near-field water as well as the temperature at the time of canister failure.

The dissolution rates of minerals or waste forms are often described by empirical formulations based on Transition State Theory (TST) and considering contributions from different factors. According to TST the dissolution rate *r* of a phase *i* can be written in simplified form as:

$$r_i = k_0 A_S e^{-E_a/RT} a_{H^+}^{n} \prod_j a_j^{n_j} f(\Delta G_r) \quad (1),$$

where k_0 is an intrinsic rate constant, A_s is the reactive surface area, E_a is the apparent activation energy of dissolution, RT is the product of the gas constant and the absolute temperature, $a(H^+)^n$ is the hydronium ion activity in solution with the reaction order n, the product term comprises the activity and reaction order of all ions in solution catalysing or inhibiting the dissolution reaction and $f(\Delta G_r)$ describes the deviation from thermodynamic equilibrium (e.g. Lasaga, 1995).

For several decades, a number of polyphase ceramics (e.g. SYNROC) and single-phase ceramic matrices have intensively been discussed as potential waste forms for the disposition of special actinide bearing nuclear waste streams, such as separated plutonium from civilian sources unsuitable for further use, surplus weapons plutonium, or minor actinides (MA: Np, Am, Cm) separated in advanced partitioning schemes (e.g. Ringwood, 1979; Donald et al., 1997; Ewing, 1999; 2007, 2011; Lumpkin, 2006; Weber et al., 2009; Deissmann et al. 2012; Donald, 2016). Besides ceramics based on zircon ($ZrSiO_4$) or zirconia (ZrO_2), titanate- and/or zirconate-based oxides (e.g. with zirconolite ($CaZrTi_2O_7$) or pyrochlore ($Ln_2(Ti,Zr,Hf)_2O_7$) structure), various phosphate-based materials, such as *Ln*-orthophosphates ($LnPO_4$) with monazite or xenotime structure, thorium-phosphate-diphosphates ($Th_4(PO_4)_4P_2O_7$), or britholites ($(Ca,Ln)_5((PO_4),(SiO_4))_3(OH,F)$) have been extensively discussed for this purpose (Boatner and Sales, 1988; Ewing and Wang, 2002; Dacheux et al., 2004; Terra et al., 2006a,b; Bregiroux et al., 2007; Oelkers and Montel, 2008; Terra et al., 2008; Vance et al., 2011; Mesbah et al., 2016; Neumeier et al., 2017a; Schlenz et al., 2018). In particular phosphate ceramics with monazite structure ($LnPO_4$, *Ln* = La to Gd) are deemed as promising waste matrices for actinide immobilisation, due to their outstanding properties, such as structural flexibility for actinide incorporation, high resilience against radiation-induced amorphisation, and high chemical durability (Boatner and Sales, 1988; Ewing and Wang, 2002; Oelkers and Montel, 2008; Clavier et al., 2011; Dacheux et al., 2013; Schlenz et al., 2013; Neumeier et al., 2017a). *Ln*-orthophosphates with monazite structure are monoclinic (space group $P2_1/n$, Z = 4), consisting of chains of alternating and edge-sharing PO_4 tetrahedra and LnO_9 polyhedra that are aligned parallel to the c-axis (Ni et al. 1995, Boatner 2002). Due to the rather large and irregular LnO_9 polyhedra exhibiting differing *Ln*-O bond-lengths, monazites can easily incorporate a large variety of cations including actinides (Clavier et al., 2011).

Several studies were carried out on the dissolution kinetics of natural monazite (Oelkers and Poitrasson, 2002) or synthetic lanthanide orthophosphates with monazite structure (Terra et al., 2003; Brandt et al. 2014; Teng et al., 2015; Arinicheva et al., 2018). These investigations revealed that the steady state dissolution rates of monazite-type materials are

several orders of magnitude lower compared to borosilicate glasses at corresponding conditions (Weber et al. 2009). However, so far only few studies were dedicated to the temperature dependence of the dissolution kinetics of monazite-type materials. Oelkers and Poitrasson (2002) studied the dissolution kinetics of natural monazite from Manangotry, Madagascar, as a function of temperature from 50 to 230°C at pH 2. Terra et al. (2003) determined the apparent activation energy of the dissolution of synthetic $GdPO_4$ with monazite structure from the normalised dissolution rates measured at room temperature and 90°C under more acidic conditions (pH = 1). The dissolution rates of monazite as function of pH follow a trend common for many minerals, with a minimum at near neutral pH, and increasing both with decreasing pH under acidic conditions, and with increasing pH at basic conditions (e.g. Oelkers and Poitrasson (2002)). Therefore, the dissolution rates, determined in acidic media to reach elemental concentrations in solution above the detection limit of available analytical techniques to obtain measurable rates, can then be extrapolated to near neutral conditions, characteristic for a given nuclear repository..

Gausse et al. (2016) demonstrated that in aqueous environments at temperatures below about 90°C, the hydrous *Ln*-orthophosphate rhabdophane ($LnPO_4 \cdot 0.667H_2O$) is more stable than the corresponding monazite-type phase. Therefore it is presumed that rhabdophane could occur as a potential neo-formed phase on the surface of monazite waste forms in contact with groundwater in a repository after failure of the waste container, potentially controlling also the release of actinide elements from the waste form (cf. du Fou de Kerdaniel et al., 2007; Mesbah et al., 2014 and 2017; Gausse et al., 2016; Neumeier et al., 2017a, Arinicheva et al. 2018).

Therefore we systematically studied the dissolution kinetics of $LaPO_4$ with the monazite structure in dynamic dissolution experiments at far from equilibrium conditions in the temperature range between 50 and 130°C in 0.01M HNO_3 to gain a deeper insight into the mechanism governing the dissolution process within the stability fields of the two different La-orthophosphate phases. The relation between the stability of La-monazite and the potentially neoformed La-rhabdophane in the dissolution experiments was investigated within the present work in the temperature range of interest by thermodynamic modelling using the Gibbs energy minimisation (GEM) approach. The aim of the present study was to quantify the temperature dependency of the dissolution rates of La-monazite and gain insight into the mechanisms governing the dissolution process within the stability fields of the different *Ln*-orthophosphate phases.

2. Materials and methods

2.1 Sample preparation

$LaPO_4$ precursor powders were prepared hydrothermally using a slight modification of the methods described by Messamy (1999) and Neumeier et al. (2016). A 3M La-nitrate solution was prepared by dissolving $La(NO_3)_3 \cdot 6H_2O$ (99.99%, Alfa Aesar, p.a.) in deionised water. Subsequently a H_3PO_4 solution (14.6M, Merck, p.a.) was added. This reaction mixture was transferred into Teflon beakers that were placed in a stainless steel autoclave (Parr Instruments) and hydrothermally treated at 200±2°C for 2 h. The synthesised powders were washed several times with deionised water, dried at 90°C, and calcined at 600°C for 2 h to remove water of crystallisation. After grinding in an agate mortar, the calcined powders were pelletised by uniaxial pressing at 445 MPa pressure and sintered at 1450°C for 5 h. The pellets were coarsely crushed and sieved in order to obtain the particle size fraction of 100 to 180 µm. These powders were additionally washed several times with deionised water in an ultrasound bath to remove finer particles from the materials surface.

2.2 Sample characterisation

The density of the sintered pellets was measured using Archimedes principle with water as immersion liquid at ambient temperature. The specific surface area of the powder samples of the particle size fraction 100 to 180 µm was determined via 5-point N_2-BET measurements using a Quantachrome Autosorb instrument. The crystal structure of the samples was confirmed by powder X-ray diffraction using a Bruker D4 Endeavor with a θ-2θ-geometry configured with a Cu-K_α target (λ = 1.54184 Å) and set to a power level of 50 kV and 30 mA. In addition, the microstructure of the samples and phase purity/composition were studied by scanning electron microscopy (SEM) using a FEI Quanta 200 FEG scanning electron microscope equipped with Genesis energy dispersive X-ray spectroscopy (EDS) system. The SEM measurements were carried out in a low-vacuum mode at 0.4 to 0.6 mbar using acceleration potentials ranging between 7 and 20 kV.

2.3 Dissolution experiments

Dynamic dissolution experiments were performed using two different experimental setups depending on the temperature conditions. A single pass flow through (SPFT) experimental set-up adapted from Dacheux et al. (2010) and Neeway et al. (2011), and used in recent studies by Brandt et al. (2014) was used for dissolution tests at 50, 60, and 80°C, respectively. The setup consists of a perfluoroalkoxy polymer (PFA) reactor (Savillex) with a total volume of 50 mL placed inside a thermostatic oil bath, and a peristaltic pump, passing the inlet

165 solution through the reactor. All experiments were carried out using 0.01M HNO_3 (Merck,
166 Suprapur®) and employing 0.8 g of monazite powder. A flow rate between 0.18 and 0.7 mL
167 min^{-1} was set and monitored by weighing the outflowing solution mass before sampling. The
168 outlet solution was sampled regularly. Samples of the outlet solution were filtered using
169 Anatop 25 plus filters with a pore size of 0.02 mm. To avoid sorption effects, the filters were
170 saturated with outlet solution before sampling. The samples were acidified by adding 1 vol%
171 HNO_3 (14.3 M, Merck, Suprapur®). The La-concentrations in the filtered and acidified
172 samples were determined by ICP-MS using an ICP-MS ELAN 6100 DRC (PerkinElmer
173 SCISX) instrument.

174 Moreover, experiments to temperatures up to 130°C were conducted in a hydrothermal
175 mixed flow setup using a reactor system similar to the one used by Oelkers and Poitrasson
176 (2002) and described in detail by Finkeldei et al. (2014). The experimental setup consisted of
177 a pressurised titanium reactor (Parr Instruments) with a total volume of 50 mL, equipped with
178 a pressure gauge, an externally driven stirring system and a thermocouple. The acidic inlet
179 solution was passed into the reactor by a high pressure liquid chromatography pump. The
180 outflow of the reactor was regulated by a computer controlled pressure valve and was filtered
181 through a Ti-cylinder frit with a pore size of 2 µm and an in-line Ti-filter with 0.5 µm pore
182 size to avoid the loss of fines. At the start of a dissolution experiment, about 0.8 g of the
183 $LaPO_4$ powder and 35 mL of 0.01 N HNO_3 (Merck) were placed into the reactor, which was
184 pressurised with He and heated up to the desired temperature. During the experiment the
185 reactor was continuously stirred at a low stirring rate of 100 rpm. The pressure was kept
186 constant by pumping fresh solution into the reactor at pump rates of 0.5 to 0.6 mL min^{-1} and
187 continuously releasing solution through the pressure valve. Samples were taken, filtered and
188 analysed in the same way as for the experiments in the SPFT experimental setup with the PFA
189 reactors.

190 Normalised steady state monazite dissolution rates (r_{mon}) were calculated from the outlet
191 solution concentrations of La ($C_{(La)}$) using the following equation:

192 $$r_{mon} = F \times C_{(La)} / X_{(La)} \times A_S \quad (2),$$

193 where F equals the fluid flow rate, $X_{(La)}$ is the stoichiometric factor representing the mass
194 fraction of La in $LaPO_4$, and A_S represents the total surface area of the powder present in the
195 reactor at the start of the experiment.

196

197 *2.4 Thermodynamic modelling*

198 The preferential stability of anhydrous and hydrated La-orthophosphate phases in the
199 temperature range from 25 to 95°C was addressed using a thermodynamic modelling
200 approach to support the interpretation of the dissolution experiments. The modelling was
201 performed using the GEM-Selektor software ver. 3.3. (Kulik et al., 2012). In GEM-Selektor,
202 the phase equilibrium is found via direct minimisation of the total Gibbs energy of the system
203 defined by its bulk elemental composition, temperature, pressure and standard Gibbs energy
204 per mole of all chemical species. The chemical thermodynamic database implemented in
205 GEM-Selektor based on SUPCRT92 (Johnson et al. 1992) and the PSI/NAGRA Chemical
206 Thermodynamic Database 12/07 (Thoenen et al., 2014) was extended to include data for the
207 relevant solid phases (cf. Table 1). Thermodynamic properties of $LaPO_4$-monazite were taken
208 from Tardy and Vieillard (1977), Popa and Konings (2006) and Neumeier et al. (2017b),
209 respectively, and added to the GEM thermodynamic database; for La-rhabdophane
210 ($LaPO_4 \cdot 0.667H_2O$) data from Gausse et al. (2016) were employed. For the thermodynamic
211 modelling an input recipe reflecting the experimental conditions in the dissolution
212 experiments was used by adding 20 g La-monazite to 1 kg 0.01 molar HNO_3 solution (i.e.
213 solid to liquid ratio 1:50). Both La-rhabdophane and La-monazite were specified as possible
214 stable phases under these conditions.

215 **Table 1**

216 Thermodynamic data for La-monazite ($LaPO_4$) and La-rhabdophane ($LaPO_4 \cdot 0.667H_2O$) used
217 for GEMS modelling. Coefficients a, b and c refer to the polynomial coefficients describing
218 the temperature dependence of the heat-capacity C_p according to $C_p = a + b \cdot 10^{-3}T - c \cdot 10^{-6}T^{-2}$.

	$\Delta G_f°$ (kJ mol^{-1})	$\Delta H_f°$ (kJ mol^{-1})	S° (J mol^{-1} K^{-1})	*a*	$b \cdot 10^3$	$c \cdot 10^{-6}$
La-monazite	-1843.8[a]	-1994.36	108.28	121.1275	30.1156	-2.5625
La-rhabdophane	-2004 ± 2	-2151 ± 13	170 ± 36			

219 [a] average value from Tardy and Vieillard (1977) and Popa and Konings (2006)

220

221 **3. Results and discussion**

222 *3.1 Sample characterisation*

223 The X-ray diffraction (XRD) pattern of the synthesised and sintered $LaPO_4$ powder is
224 depicted in Fig. 1. According to XRD, single-phase $LaPO_4$-monazite of high crystallinity was

obtained after the sintering step. The EDX analyses performed on sintered pellets revealed that, within the error of the applied analytical method, the synthesised La-monazite is chemically homogeneous and lacking any zonation. The density of the sintered pellets reached about 96% of the theoretical density of $LaPO_4$. SEM observations on powders used in the dissolution experiments (100 – 180 µm fraction) indicated that the particles are made up of well sintered grains up to 30 µm in size with trapped intragranular pores of sub-micrometric size with minor intergranular porosity in the grain interstices (Fig. 2). The N_2-BET surface area of the powder used in the dissolution experiments was 0.4 ± 0.1 m^2 g^{-1}.

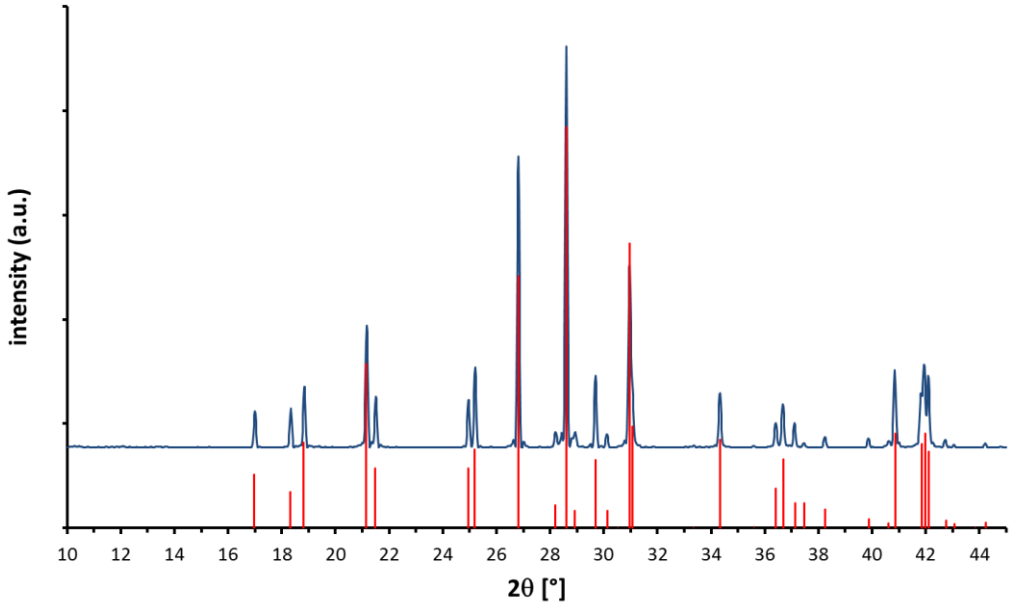

Fig. 1. XRD-pattern of sintered $LaPO_4$ powder showing the presence of single-phase La-monazite (Reference data monoclinic $LaPO_4$, COD ID 9001647).

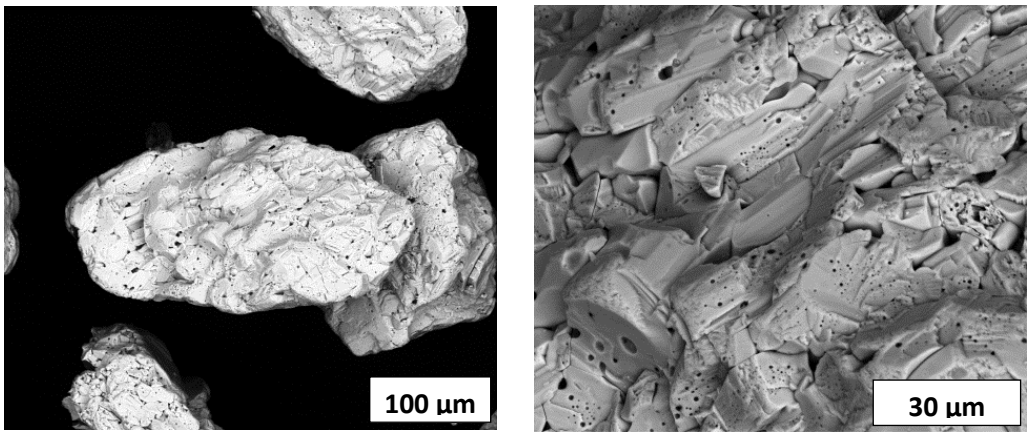

Fig. 2. Backscattered electron SEM micrographs of the sieved $LaPO_4$-powder used in the dissolution experiments.

3.2 Dissolution kinetics

The La-concentrations obtained in the dynamic dissolution experiments at temperatures between 50 and 130°C are provided in Tables S1 and S2 in the supplemental information. In particular in experiments performed at temperatures below 90°C, the dissolution experiments followed the typical trend of dynamic dissolution experiments as frequently described in the literature (e.g. Oelkers and Poitrasson, 2002, Brandt et al., 2003; Horlait et al., 2012; Finkeldei et al., 2013 and 2014). In the initial stages of the experiments, higher dissolution rates were observed that decrease with time until a steady state, i.e. a constant rate with time, was reached. Steady state dissolution rates were approached within one week for all temperatures. The higher initial dissolution rates are generally thought to be due to dissolution of fine particles adhering to the materials surface and/or dissolution at highly reactive surface sites created during the crushing of the pellets (e.g. Chou and Wollast, 1984; Knauss and Thomas, 1989; Wehrli, 1989; Casey and Bunker, 1990; Oelkers and Poitrasson, 2002; Horlait et al., 2012). An alternative explanation for the enhanced initial dissolution rates proposed by Luettge et al. (2013) is related to changes of the dominating dissolution mechanism e.g., from dissolution at grain boundaries to the dissolution on steps, kinks and etch pits on grain surfaces.

The steady state dissolution rates of the $LaPO_4$ monazite powders are summarised in Table 2. Within the temperature interval from 50 to 130°C, the normalised dissolution rates increased by roughly one order of magnitude from 3.2×10^{-5} to 2.5×10^{-4} $g\cdot m^{-2}\cdot d^{-1}$. The dissolution rates obtained using the two different experimental setups at the same temperatures are in a good agreement.

Table 2

Normalised dissolution rates of $LaPO_4$ in 0.01M HNO_3 at different temperatures using two different experimental setups.

T °C	r_{mon} ($g\cdot m^{-2}\cdot d^{-1}$) PFA-reactor / SPFT	r_{mon} ($g\cdot m^{-2}\cdot d^{-1}$) Ti-reactor / mixed flow
50	$3.20\times10^{-5} \pm 2\times10^{-7}$	
60	$4.60\times10^{-5} \pm 3\times10^{-7}$	$3.6\times10^{-5} \pm 3\times10^{-6}$
80	$8.5\times10^{-5} \pm 9\times10^{-6}$	$1.200\times10^{-4} \pm 2\times10^{-7}$
90	$1.8\times10^{-4} \pm 5\times10^{-5}$ [a]	$2.20\times10^{-4} \pm 4\times10^{-6}$

110	$2.0\times10^{-4} \pm 2\times10^{-5}$
130	$2.5\times10^{-4} \pm 1\times10^{-5}$

[a] data from Brandt et al. 2014

The normalised dissolution rates of $LaPO_4$ obtained in our study correspond rather well to data derived for various other natural or synthetic monazites. Oelkers and Poitrasson (2002) determined dissolution rates of 9.3×10^{-6} and ~2.2×10^{-5} g m^{-2} d^{-1} for natural Ce-monazite from Manangotry, Madagascar, under dynamic conditions at 50 and 70°C at pH ~2, respectively. Terra et al. (2003) measured dissolution rates of synthetic $GdPO_4$ with monazite structure of 3.8×10^{-4} to 5.9×10^{-4} g m^{-2} d^{-1} at 90°C at pH 1. Slightly higher dissolution rates of 1.7×10^{-3} g m^{-2} d^{-1} were obtained by Brandt et al. (2014) for synthetic Eu-monazite at 90°C and pH 2 in SPFT experiments. In this study, within the solid-solution series $LaPO_4$ – $EuPO_4$, a minimum of the dissolution rate (5.8×10^{-5} g m^{-2} d^{-1}) was observed at an $EuPO_4$ mole fraction of 0.2. Teng et al. (2015) investigated the dissolution behaviour of synthetic $Ce_{0.5}Eu_{0.5}PO_4$ with monazite structure at 90°C in deionised water. They found normalised elementary release rates of Ce and Eu below 4×10^{-5} and 2×10^{-4} g m^{-2} d^{-1}, respectively, after 21d. Veilly (2008) determined the dissolution kinetics of Th-cheralite ($CaTh(PO_4)_2$), a monoclinic monazite type phase with similar lattice parameters compared to $LaPO_4$, in dynamic dissolution experiments at 90 C and pH 1, reporting a Th-based dissolution rate of 2.2×10^{-5} g m^{-2} d^{-1}.

Based on the dissolution rates obtained at constant pH and at far from equilibrium conditions, the apparent activation energy of the dissolution process can be determined according to the Arrhenius' law, where:

$$r_{mon} \propto e^{-E_a/RT} \quad (3),$$

with the activation energy E_a, the gas constant R, and the absolute temperature T. Using a simple mathematical transformation equation (3) takes the form:

$$\ln(r_{mon}) = -(E_a/R)(1/T) + lnA \quad (4),$$

where A is the pre-exponential factor of the Arrhenius equation. In the Arrhenius plot (Fig. 3) two different linear trends can be observed for the temperature dependence of the dissolution rates of $LaPO_4$ under acidic conditions, suggesting changes in the rate limiting step in the overall dissolution mechanism. From the slopes of the regression lines, apparent activation energies of 44 ± 5 and 7.5 ± 4.3 kJ mol^{-1} were determined for the temperature ranges 50 to 90°C and 90 to 130°C, respectively.

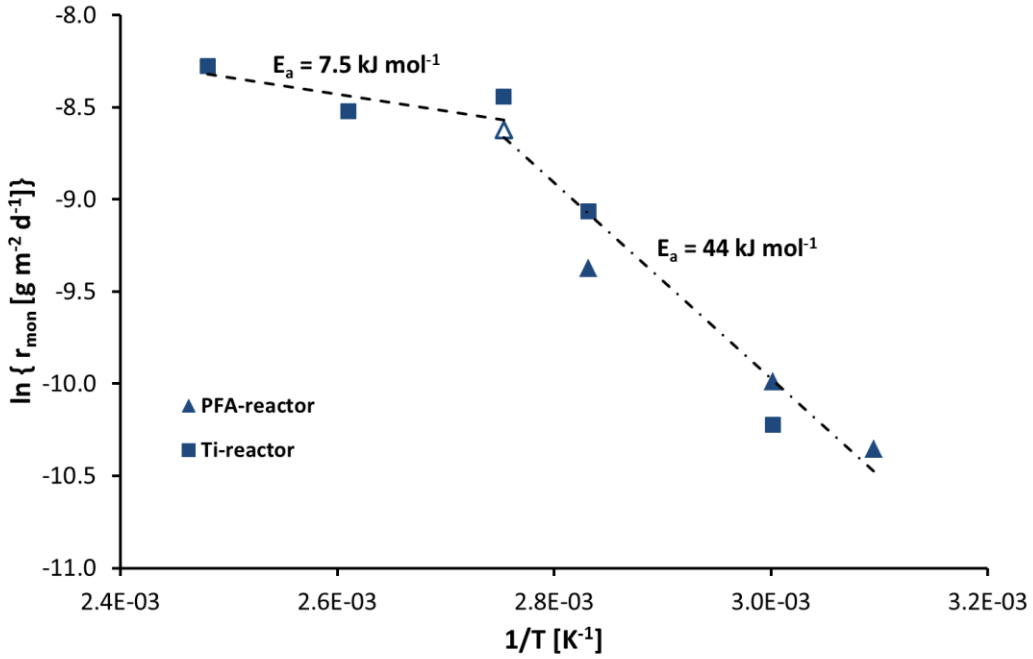

294

295 **Fig. 3.** Arrhenius plot of the dissolution rates of $LaPO_4$ as function of reciprocal temperature.
296 The open triangle corresponds to the dissolution rate from Brandt et al. (2014).

297 These values of apparent activation energies allow for an evaluation of the mechanisms of
298 the overall dissolution reactions. According to literature, the apparent activation energy of
299 surface-reaction controlled dissolution (E_a from ~40 to 140 kJ mol^{-1}) is distinctively higher
300 than for transport-controlled dissolution (E_a less than ~20 kJ mol^{-1}) (cf. Locker and de Bruy,
301 1969; Lasaga, 1981 and 1984; Deng, 1997; Langmuir, 1997). This suggests that the
302 dissolution of the $LaPO_4$ ceramics proceeds via a surface-reaction controlled mechanism at
303 temperatures below 90°C and via a transport-controlled dissolution mechanism at higher
304 temperatures. Similar results revealing two different mechanisms for the dissolution of *Ln*-
305 orthophosphate ceramics depending on temperature were obtained by Gausse (2016) in
306 dynamic dissolution experiments. In this study apparent activation energies of 79 ± 8 kJ mol^{-1}
307 (T: 25 to 40°C) and 13 ± 1 kJ mol^{-1} (T: 40 to 90°C) for the dissolution of $LaPO_4$ were
308 determined (Gausse, 2016), suggesting similarly a surface-reaction controlled dissolution
309 mechanism at lower temperatures and a transport controlled dissolution mechanism at
310 elevated temperature. The higher apparent E_a determined in the temperature range 25 to 40 °C
311 by Gausse (2016) and the different temperature ranges for the two prevailing dissolution
312 mechanisms observed by Gausse (2016) in comparison to our work, might be due to the less
313 acidic conditions in our experiments (cHNO3 =0.1 (Gausse (2016) vs. cHNO3 = 0.01 M (this work)),
314 and the fact that only two data points were used for the determination of E_a.

315 Different dissolution mechanisms as function of temperature have been also reported
316 previously with respect to the leaching kinetics of brannerite (nominally UTi_2O_6) ores (Born,
317 1975; Gogoleva, 2012). In the low temperature range from 15 to 35°C, an apparent activation
318 energy of 50.5 kJ·mol^{-1} was determined, typically for surface-reaction controlled dissolution
319 mechanisms. Between 35 and 90°C, a decrease of the apparent activation energy down to 30.3
320 kJ·mol^{-1} was reported. Gogoleva (2012) assigned this value to a mix of two mechanisms, i.e.
321 surface-reaction and product layer diffusion.

322 Terra et al. (2003) evaluated an apparent activation energy of 39 to 45 kJ mol^{-1} for the
323 dissolution of synthetic $GdPO_4$ with monazite structure from the values of the normalised
324 dissolution rates at 90°C and room temperature, in line with our value for $LaPO_4$ below 90°C.
325 In contrast, Oelkers and Poitrasson (2002) determined the apparent activation energy
326 associated with the dissolution of natural Ce-monazite from Manangotry, Madagaskar, to be
327 41.8 ± 12.6 kJ mol^{-1} in the entire temperature range from 50 to 230°C at pH = 2, without
328 observing any change in the E_a value. However, Oelkers and Poitrasson (2002) studied natural
329 monazite samples with very complex elemental composition, containing both, various
330 lanthanide (Ce, La, Nd) and actinide (Th, U) cations, as well as SiO_4^{3-} and PO_4^{3-} anions. Du
331 Fou de Kerdaniel et al. (2007) demonstrated the influence of the chemical composition of the
332 *Ln*-orthophosphates on the temperature range of stability of rhabdophane-type compounds
333 phases, which might explain the absence of two different dissolution mechanisms in the
334 experiments of Oelkers and Poitrasson (2002).

335 *3.3 Thermodynamic modelling*

336 In Fig. 4, the results of the thermodynamic modelling of the dissolution of $LaPO_4$-
337 monazite in an acidic aqueous solution (0.01M HNO_3) at various temperatures are shown. The
338 calculated La concentrations in solution depict the retrograde solubility of *Ln*-orthophosphates
339 (cf. Poitrasson et al., 2004; Cetiner et al. 2005) with La-concentrations decreasing from about
340 $3.7 \cdot 10^{-5}$ mol L^{-1} to about $1.5 \cdot 10^{-5}$ mol L^{-1} in the temperature interval from 30 to 97°C.
341 Moreover, the thermodynamic calculations with GEM-Selektor revealed that La-rhabdophane
342 is the thermodynamically stable phase in this temperature range. Scoping calculations at
343 higher temperatures indicate that above about 102°C (375 K) La-monazite is the
344 thermodynamically favoured La-orthophosphate phase (cf. Fig. 4). This is consistent with the
345 experimental findings of du Fou de Kerdaniel et al. (2007), who observed in synthesis from
346 oversaturation conditions, the formation of La-monazite at and above 373 K, whereas at
347 temperatures below 363 K, La-rhabdophane occurred. In contrast, Cetiner et al. (2005)

concluded from PXRD data that the solid phase used in experiments to determine the solubility product of $LaPO_4$ from under-saturation at 23°C and 50°C had the monazite structure before and after the experiment. However, this can probably be explained by the very low amount of neoformed rhabdophane during the dissolution experiment, which cannot be evidenced by PXRD (cf. Gausse, 2016).

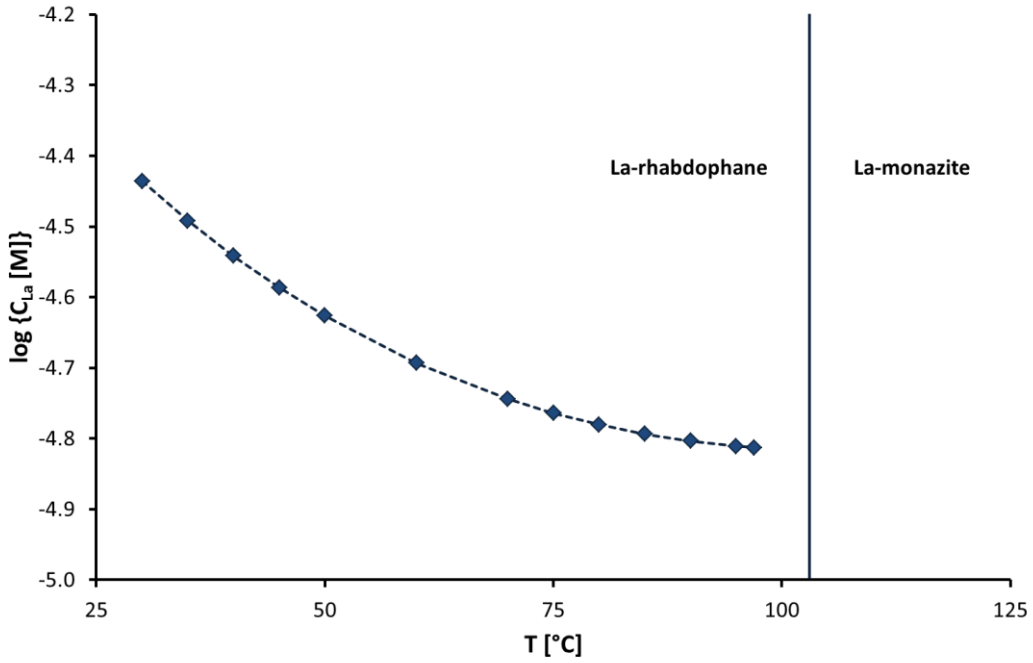

Fig. 4. La-concentrations in equilibrium with a solid La-orthophosphate phase in 0.01M HNO_3 calculated with GEM-Selektor and estimated predominance fields of La-rhabdophane and La-monazite as function of temperature.

The estimated border between the predominance fields of the different La-orthophosphates is thus in the same temperature range as the observed change in the dissolution mechanism. This suggests that the different dissolution mechanisms might be influenced by the hydration of monazite and the formation of a thin rhabdophane layer on the sample surface as an intermediate step controlling the dissolution in the temperature range below about 90 to 100°C, whereas the dissolution behaviour at elevated temperatures is controlled by direct dissolution of La-monazite.

4. Conclusions

The temperature dependence of the dissolution kinetics of sintered La-phosphate ceramics with monazite structure was studied, to gain a more detailed insight into the mechanisms governing the dissolution of monazite-type ceramics proposed as nuclear waste forms for

actinide immobilisation. Pure single-phase La-monazite was obtained from precursors synthesised via a hydrothermal route after calcination and sintering. The dissolution kinetics of sintered La-phosphate powders were studied in dynamic dissolution experiments in the temperature range from 50 to 130°C under acidic conditions (0.01M HNO_3). The overall dissolution rates at far from equilibrium conditions increased by roughly one order of magnitude from 3.2×10^{-5} to 2.5×10^{-4} g m^{-2} d^{-1} in this temperature interval. The dissolution rates are in a similar range as those reported from dynamic experiments with natural and synthetic monazite in the literature. In the Arrhenius plot, two different temperature regions were observed, in which the normalised dissolution rates of $LaPO_4$ show a distinctively different dependence on temperature, indicating two different mechanisms of dissolution: surface-controlled dissolution at lower temperature (T = 50 – 90°C; E_a = 44 kJ·mol^{-1}) and transport-controlled dissolution at higher temperature (T = 90 – 130°C; E_a = 7.5 kJ·mol^{-1}). Complementary thermodynamic modelling reflecting the experimental conditions in the dissolution experiments demonstrated that La-rhabdophane ($LaPO_4$·$0.667H_2O$) is the thermodynamically favoured phosphate phase in aqueous environments below about 100°C, whereas at higher temperatures La-monazite is the thermodynamically stable La-orthophosphate. Based on these results, it is proposed that the dissolution rates and activation energy reported here for temperatures below 90°C refer not directly to the dissolution of La-monazite but to the formation and dissolution of a thin layer of La-rhabdophane formed at the monazite surface, including potentially a hydration step. Hence, rhabdophane-type phases might control the dissolution kinetics of *Ln*-orthophosphate-based ceramic waste forms under conditions relevant to geological disposal. Taking into account the dependency of the temperature of the rhabdophane-monazite transition on the cation radius described by du Fou de Kerdaniel et al. (2007), the transition temperature for An^{III}-bearing La-monazite waste forms (An^{III} = Pu^{III}, Am^{III}, Cm^{III}) would be higher than the temperature calculated here for the pure La-phosphate-system. Thus for an *An*-bearing La-monazite waste form generally the dissolution behaviour of the rhabdophane phase is the relevant issue under repository conditions.

Acknowledgement

The research leading to these results received financial support from the German Federal Ministry of Education and Research (BMBF) within the collaborative research project "Conditioning" (grant 02NUK021A).

References

Ahn, J., Apted, M. J. 2011. Geological repository systems for safe disposal of spent nuclear fuels and radioactive waste. Woodhead Publishing, Oxford.

Arinicheva, Y., Neumeier, S., Brandt, F., Bosbach, D., Deissmann, G. 2018. Dissolution kinetics of synthetic $LaPO_4$-monazite in acidic media. MRS Advances, https://doi.org/10.1557/adv.2018.205.

Boatner, L.A. 2002. Synthesis, structure and properties of monazite, pretulite and xenotime. Rev. Miner. Geochem. 48, 87-121.

Boatner, L., Sales, B. 1988. Monazite. In: W. Lutze, R.C. Ewing (eds.) Radioactive waste forms for the future. North Holland, Amsterdam, pp. 495-564.

Born, C.A., Queneau, P.B., Ronzio, R.A. 1975. Processing of wolframite-cassiterite concentrate for brannerite removal. Trans Soc. Min. Eng., AIME 258, 218-221.

Brandt, F., Bosbach, D., Krawczyk-Bärsch, E., Arnold, T., Bernhard, G., 2003. Chlorite dissolution in the acid pH-range: a combined microscopic and macroscopic approach. Geochim. Cosmochim. Acta 67, 1451-1461.

Brandt, F., Neumeier, S., Schuppik, T., Arinicheva, Y., Bukaemskiy, A., Modolo, G., Bosbach, D. 2014. Conditioning of minor actinides in lanthanum monazite ceramics: A surrogate study with Europium. Prog. Nucl. Energy 72, 140-143.

Bregiroux, D., Terra, O, Audubert, F., Dacheux, N., Serin, V., Podor, R., Bernache-Assollant, D. 2007. Solid-state synthesis of monazite-type compounds containing tetravalent elements. Inorg. Chem. 46, 10372-10382.

Casey, W.H., Bunker, B. 1990. Leaching of mineral and glass surfaces during dissolution. Rev. Miner. 23, 397-426.

Cetiner, Z.S., Wood, S.A., Gammons, C.H. 2005. The aqueous geochemistry of the rare earth elements. Part XIV. The solubility of rare earth element phosphates from 23 to 150 °C. Chem. Geol. 217, 147-169.

Chou, L., Wollast, R. 1984. Study of weathering of albite at room-temperature and pressure with a fluidized-bed reactor. Geochim. Cosmochim. Acta 48, 2205-2217.

Clavier, N., Podor, R., Dacheux, N. 2011. Crystal chemistry of the monazite structure. J. Europ. Ceram. Soc. 31, 941-976.

Council of the European Union 2011. COUNCIL DIRECTIVE 2011/70/EURATOM of 19 July 2011 establishing a Community framework for the responsible and safe management of spent fuel and radioactive waste. Brussels, 56 pp.

Dacheux, N., Clavier, N., Robisson, A.C., Terra, O., Audubert, F., Lartigue, J.E., Guy, C. 2004. Immobilisation of actinides in phosphate matrices. C. R. Chimie 12, 1141-1152.

Dacheux, N., de Kerdaniel, E.D.F., Clavier, N., Podor, R., Aupiais, J., Szenknect, S. 2010. Kinetics of dissolution of thorium and uranium doped britholite ceramics. J. Nucl. Mater. 404, 33-43.

Dacheux, N., Clavier, N., Podor, R. 2013. Versatile monazite: resolving geological records and solving challenges in materials science. Monazite as a promising long-term radioactive waste matrix: benefits of high-structural flexibility and chemical durability. Am. Mineral. 98, 833-847.

Deissmann, G., Neumeier, S., Modolo, G., Bosbach, D. 2012. Durability of potential plutonium wasteforms under repository conditions. Min. Mag. 76, 2911-2918.

Deng, Y. 1997. Effect of pH on the reductive dissolution rates of iron(III) hydroxide by ascorbate. Langmuir 13, 1835-1839.

Donald, I.W. 2016. Waste immobilization in glass and ceramic based hosts: Radioactive, toxic and hazardous Wastes, John Wiley & Sons Ltd, Chichester.

Donald, I.W., Metcalfe, B.L., Taylor, R.N.J. 1997. Review: the immobilisation of high level radioactive wastes using glasses and ceramics. J. Mater. Sci. 32, 5851-5887.

du Fou de Kerdaniel, E., Clavier, N., Dacheux, N., Terra, O., Podor, R. 2007. Actinide solubility-controlling phases during the dissolution of phosphate ceramics. J. Nucl. Mater. 362, 451-458.

Ewing, R.C. 1999. Ceramic matrices for plutonium disposition. Proc. Nat. Acad. Sci. USA 96, 3432-3439.

Ewing, R.C., Wang, L. 2002. Phosphates as nuclear waste forms. Rev. Miner. Geochem. 48, 673-699.

Ewing, R.C. 2007. Ceramic matrices for plutonium disposition. Prog. Nucl. Energy 49, 635-643.

Ewing, R.C. 2011. Actinides and radiation effects: impact on the back-end of the nuclear fuel cycle. Min. Mag. 75, 2359-2377.

Finkeldei, S., Brandt, F., Bukaemskiy, A., Neumeier, S., Modolo, G., Bosbach, D. 2013. Synthesis and dissolution kinetics of zirconia based ceramics. Prog. Nucl. Energy, 72, 130-133.

Finkeldei, S., Brandt, F., Rozov, K., Bukaemskiy, A. A., Neumeier, S., Bosbach, D. 2014. Dissolution of ZrO_2 based pyrochlores in the acid pH range: A macroscopic and electron microscopy study. Appl. Geochem. 49, 31-41.

Gausse, C. 2016. Synthèse et dissolution de matrices phosphatées de structure monazitique. PhD Thesis, Université de Montpellier.

Gausse, C., Szenknect, S., Qin, D.W., Mesbah, A., Clavier, N., Neumeier, S., Bosbach, D., Dacheux, N. 2016. Determination of the solubility of rhabdophanes $LnPO_4 \cdot 0.667H_2O$ (Ln = La to Dy). Eur. J. Inorg. Chem. 2016, 4615-4630.

Gogoleva, E.M. 2012. The leaching kinetics of brannerite ore in sulfate solutions with iron(III). J. Radioanal. Nucl. Chem. 293, 183-191.

Horlait, D., Tocino, F., Clavier, N., Dacheux, N., Szenknect, S. 2012. Multiparametric study of $Th_{1-x}Ln_xO_{2-x/2}$ mixed oxides dissolution in nitric acid media. J. Nucl. Mater. 429, 237-244.

International Atomic Energy Agency (IAEA) 2004: Scientific and technical basis for the geological disposal of radioactive wastes. Technical Reports Series 413, Vienna, 80 pp.

Johnson, J.W., Oelkers, E.H., Helgeson, H.C. 1992. SUPCRT92: A software package for calculating the standard molal thermodynamic properties of minerals, gases, aqueous species, and reactions from 1 to 5000 bar and 0 to 1000°C. Comput. Geosci. 18, 899-947.

Knauss, K.G., Thomas, J.W. 1989. Muscovite dissolution kinetics as a function of pH and time at 70°C. Geochim. Cosmochim. Acta 53, 1493-1501.

Kulik, D.A., Wagner, T. Dmytrieva, S.V., Kosakowski, G., Hingerl, F.F., Chudnenko, K.V. Berner, U.R. 2013. GEM-Selektor geochemical modeling package: revised algorithm and GEMS3K numerical kernel for coupled simulation codes. Computat. Geosci. 17, 1-24.

Langmuir, D. 1997. Aqueous environmental geochemistry. Prentice Hall, Upper Saddle. River, New Jersey.

Lasaga, A.C. 1981. Rate laws of chemical eeactions. Rev. Miner. 8, 1-68.

Lasaga, A.C. 1984. Chemical kinetics of water-rock interactions. J. Geophys. Res. B: Solid Earth 89: 4009-4025.

Lasaga, A.C. 1995. Fundamental approaches in describing mineral dissolution and precipitation rates. Rev. Mineral. Geochem. 31, 23-86.

Locker, L.D., de Bruy, P.L. 1969. The kinetics of dissolution of II-VI semiconductor compounds in nonoxidizing acids. J. Electrochem. Soc. 116, 1658-1665.

Luettge, A., Arvidson, R.S., Fischer, C. 2013. A stochastic treatment of crystal dissolution kinetics. Elements 9, 183-188.

Lumpkin, G.R. 2006. Ceramic waste forms for actinides. Elements 2, 365-372.

Mesbah, A., Clavier, N., Elkaim, E., Gausse, C., Kacem, I.B., Szenknect, S., Dacheux, N. 2014. Monoclinic form of the rhabdophane compounds: $REEPO_4{\cdot}0.667H_2O$. Cryst. Growth Des. 14, 5090-5098.

Mesbah, A., Clavier, N., Lozano-Rodriguez, M.J., Szenknect, S., Dacheux, N. 2016. Incorporation of thorium in the zircon structure type through the $Th_{1-x}Er_x(SiO_4)_{1-x}(PO_4)_x$ thorite−xenotime solid solution. Inorg. Chem. 55, 11273-11282.

Mesbah, A., Clavier, N., Elkaim, E., Szenknect, S., Dacheux, N. 2017. In pursuit of the rhabdophane crystal structure: from the hydrated monoclinic $LnPO_4.0.667H_2O$ to the hexagonal $LnPO_4$ (Ln = Nd, Sm, Gd, Eu and Dy). J. Solid State Chem. 249, 221-227.

Messamy, H., Riwotzki, K., Kornowski, A., Naused, S., Haase, M. 1999. Wet-chemical synthesis of doped colloidal nanomaterials particles and fibers of $LaPO_4$:Eu, $LaPO_4$:Ce, and $LaPO_4$:Ce,Tb. Adv. Mater. 11, 840-844.

Neeway, J., Abdelouas, A., Grambow, B., Schumacher, S. 2011. Dissolution mechanism of the SON68 reference nuclear waste glass: New data in dynamic system in silica saturation conditions. J. Nucl. Mater. 415, 31-37.

Neumeier, S., Arinicheva, Y., Clavier, N., Podor, R., Bukaemskiy, A., Modolo, G., Dacheux, N. Bosbach, D. 2016. The effect of the synthesis route of monazite precursors on the microstructure of sintered pellets. Prog. Nucl. Energy 92: 298-305.

Neumeier, S., Arinicheva, Y., Ji, Y., Heuser, J.M., Kowalski, P.M., Kegler, P., Schlenz, H., Bosbach, D., Deissmann, G. 2017a. New insights into phosphate based materials for the immobilisation of actinides. Radiochim. Acta 105, 961-984.

Neumeier, S., Kegler, P., Arinicheva, Y. Shelyug, A., Kowalski, P. M., Schreinemachers, C., Navrotsky, A., Bosbach, D. 2017b. Thermochemistry of $La_{1-x}Ln_xPO_4$-monazites (Ln=Gd, Eu). J. Chem. Thermodynamics 105, 396-403.

Ni, Y.X., Hughes, J.M., Mariano, A.N. 1995. Crystal chemistry of the monazite and xenotime structure. Am. Mineral. 80, 21-26.

Oelkers, E.H., Poitrasson, F. 2002. An experimental study of the dissolution stoichiometry and rates of a natural monazite as a function of temperature from 50 to 230^{o}C and pH from 1.5 to 10. Chem. Geol. 191, 73-87.

532 Oelkers, E., Montel, J.-M. 2008. Phosphates and nuclear waste storage. Elements 4, 113-116.

533 Poitrasson, F., Oelkers, E., Schott, J., Montel, J.-M. 2004. Experimental determination of
534 synthetic $NdPO_4$ monazite end-member solubility in water from 21°C to 300°C:
535 implications for rare earth element mobility in crustal fluids. Geochim. Cosmochim. Acta
536 68, 2207-2221.

537 Popa, K., Konings, R.J.M. 2006. High-temperature heat capacities of $EuPO_4$ and $SmPO_4$
538 synthetic monazites. Thermochim. Acta 445, 49-52.

539 Ringwood, A. E., Kesson, S. E., Ware, N. G., Hibberson, W., Major, A. 1979. Immobilisation
540 of high level nuclear reactor wastes in SYNROC. Nature 278, 219-223.

541 Schlenz, H., Heuser, J., Neumann, A., Schmitz, S., Bosbach, D. 2013. Monazite as a suitable
542 actinide waste form. Z. Kristallog. – Cryst. Mater. 228, 113-123.

543 Schlenz, H., Neumeier, S., Hirsch, A., Peters, L., Roth, G. 2018. Phosphates as safe containers
544 for radionuclides. In: Heuss-Aßbichler, S., Amthauer, G., John, M. (eds.) Highlights in
545 applied mineralogy. De Gruyter, Berlin, pp. 171-196.

546 Tardy, Y., Vieillard, P. 1977. Relationships among Gibbs free energies and enthalpies of
547 formation of phosphates, oxides and aqueous ions. Contrib. Mineral. Petrol. 63, 75-88.

548 Teng, Y., Wang, X., Huang, Y., Wu, L., Zeng, P. 2015. Hot-pressure sintering, microstructure
549 and chemical durability of $Ce_{0.5}Eu_{0.5}PO_4$ monazite ceramics. Ceram. Int. 41, 10057-
550 10062.

551 Terra, O., Clavier, N., Dacheux, N., Podor, R. 2003. Preparation and characterization of
552 lanthanum–gadolinium monazites as ceramics for radioactive waste storage. New J.
553 Chem. 27, 957-967.

554 Terra, O., Dacheux, D., Audubert, F., Podor, R. 2006a. Immobilization of tetravalent actinides
555 in phosphate ceramics. J. Nucl. Mater. 352, 224-232.

556 Terra, O., Audubert, F., Dacheux, N., Guy, C., Podor, R. 2006b. Synthesis and
557 characterization of thorium-bearing britholites. J. Nucl. Mater. 354, 49-65.

558 Terra, O., Dacheux, D., Clavier, N., Podor, R., Audubert, F. 2008. Preparation of optimized
559 uranium and thorium bearing brabantite or monazite/brabantite solid solutions. J. Amer.
560 Ceram. Soc. 91, 3673-3682.

561 Thoenen, T., Hummel, W, Berner, U., Curti, E. 2014. The PSI/Nagra Chemical
562 Thermodynamic Database 12/07. NAGRA Arbeitsbericht NAB 14-49.

563 Vance, E.R., Zhang, Y., McLeod, T., Davis, J. 2011. Actinide valences in xenotime and
564 monazite. J. Nucl. Mater. 409, 221-224.

565 Veilly, E. 2008. Comparative behavior of britholites and monazite-brabantite solid solutions
566 during dissolution tests: a combined experimental and DFT approach. Inorg. Chem. 47,
567 10971-10979.

568 Weber, W.J., Navrotsky, A., Stefanovsky, S., Vance, E., Vernaz, E. 2009. Materials science
569 of high-level nuclear waste immobilization. MRS Bull. 34, 46-53.

570 Wehrli, B. 1989. Monte Carlo simulations of surface morphologies during mineral
571 dissolution. J. Colloid Interface Sci. 132, 230-242.